

First astronomical application of postdetection turbulence compensation: images of α Aurigae, ν Ursae Majoris, and α Geminorum using self-referenced speckle holography

John D. Gonglewski, D. G. Voelz, J. S. Fender, D. C. Dayton, B. K. Spielbusch, and R. E. Pierson

John Gonglewski, D. G. Voelz, and J. S. Fender are with U.S. Air Force, New Mexico 87117; the other authors are with Applied Technology Associates, Inc., 1900 Randolph S. E., Albuquerque, New Mexico 87106.

Received 25 May 1990.

Sponsored by David L. Fried, Optical Sciences Company.

We describe a postdetection turbulence compensation technique for obtaining high resolution imagery through the atmosphere. We present preliminary results from field experiments.

It is well known that atmospheric turbulence typically limits the angular resolution of ground-based astronomical images to ~ 1 sec of arc.¹ Compensated imaging systems are one solution to the problem of obtaining higher resolution images through the atmosphere.² Alternatively, a technique known as speckle interferometry was developed by Labeyrie³ who discovered that high resolution autocorrelations of an object could be produced from many short exposure image frames obtained with a narrow bandwidth filter.⁴ Modifications of the speckle interferometry technique were subsequently developed that allowed real images to be reconstructed from these short exposure frames.⁵ One modification, referred to as speckle holography, uses an unresolved star near the object of interest as a reference source in much the same way a reference beam is used in conventional holography recordings.⁶⁻⁸

In this Communication, we describe our implementation of another method: a postdetection turbulence compensation technique for obtaining high resolution imagery through the atmosphere. We then present preliminary results from experiments performed in Feb. 1990 at the University of New Mexico's Capilla Peak Observatory.

For this technique, the turbulence degraded image is recorded at the same time as an estimate of the atmospheric transfer function. A compensated image is then produced through a digital deconvolution. We refer to the technique as self-referenced speckle holography (SRSH) since the object under observation acts as the reference source for a turbulence estimate, eliminating the need for an unresolved star. We use a Shack-Hartmann wavefront sensor placed at a point conjugate to the entrance pupil of a telescope to construct a reference image for an estimate of the atmospheric turbulence.

The construction of a reference image using a Shack-Hartmann wavefront sensor has been described extensively in the literature.^{9,10} Briefly, atmospheric distortions can be modeled as a single layer of phase distortion provided scintillation is not too great.¹¹ These phase distortions act as localized tilts, and the wavefront at the entrance pupil of a

telescope is sampled by an array of small lenses (lenslets). The displacement of the spot focused by each lenslet can be used to determine the local tilt of the wavefront. This information can then be used to estimate the optical transfer function of the atmosphere and telescope. Due to the small diameter of the lenslets, even objects of large angular extent appear unresolved. Thus, even an extended object can act as a point reference, eliminating the need for a reference source external to the object. The technique is similar to compensated imaging systems which use a Shack-Hartmann sensor to drive a deformable mirror; however, in our case the compensation is done via postdetection computer processing.

SRSH is not a new imaging method, although it has never been applied to astronomical objects until now. McGlamery measured point spread functions in the laboratory and used them to correct laboratory images in 1967.¹² In 1974, he simulated deconvolution imaging on a computer for both predetection and postdetection compensation cases.¹³ Fried described a practical SRSH system in 1987,¹⁰ and there have been recent laboratory demonstrations in which a wavefront sensor has been used to obtain the turbulence estimate.¹⁴

The theory of SRSH is simple. The intensity distribution $I(x,y)$ of a short exposure image frame can be described as

$$I(x,y) = O(x,y) \otimes H(x,y), \quad (1)$$

where $O(x,y)$ is the object's incoherent brightness distribution, the \otimes denotes a convolution, and $H(x,y)$ is the combined system and atmospheric point spread function (psf). The Fourier transform of $I(x,y)$ is, therefore,

$$\tilde{I}(u,v) = \tilde{O}(u,v)\tilde{H}(u,v), \quad (2)$$

where the symbol $\tilde{}$ indicates a Fourier transform, and u and v are spatial frequency variables. If the function $\phi(u,v)$ describes the phase disturbance at the pupil of the imaging system and $P(u,v)$ is the pupil intensity function, then

$$\tilde{H}(u,v) = P(u,v) \exp(2\pi j\phi) \otimes P(u,v) \exp(2\pi j\phi), \quad (3)$$

where \otimes denotes an autocorrelation. Thus, if $\phi(u,v)$ can be measured and $P(u,v)$ is known, the object can be estimated using an inverse filter of the form

$$\tilde{O}(u,v) = \frac{\tilde{I}(u,v)\tilde{H}^*(u,v)}{\tilde{H}(u,v)\tilde{H}^*(u,v) + \epsilon^2}, \quad (4)$$

where ϵ^2 is a parametric constant that prevents singularities in the recovered object by insuring that the denominator of Eq. (4) is never zero. The form of Eq. (4) is analogous to the classical constrained least-squares solution for deconvolution assuming additive noise. Equation (4) also has a Wiener filter analog, if the power spectrum of the object is known.

Equation (4) is used when a reconstruction is made from only one focal plane/psf image pair. Multiple image pairs can be used to obtain a better reconstruction. In this case the estimation algorithm is¹⁴

$$\tilde{O}(u,v) = \frac{\langle \tilde{I}(u,v)\tilde{H}^*(u,v) \rangle}{\langle \tilde{H}(u,v)\tilde{H}^*(u,v) \rangle + \epsilon^2}, \quad (5)$$

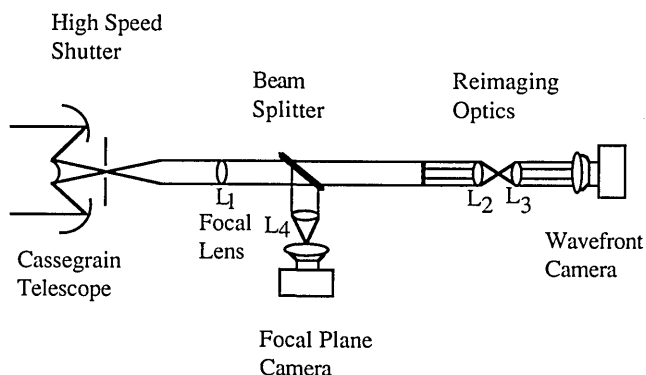


Fig. 1. Layout of self-referenced speckle holography instrument.

where the brackets denote an ensemble average.

A schematic diagram of the SRS instrument is shown in Fig. 1. The lens L_1 recollimates the light exiting the telescope. A beam splitter reflects a narrow spectral portion of the incoming light to lens L_4 , where it is focused onto the detector array of the focal plane camera. The rest of the light passes through the beam splitter to the Shack-Hartmann array. As a result, the focal plane images are speckle interferograms. The wavefront sensor is placed at a point conjugate to the telescope entrance pupil, and the output from this array is reimaged onto the detector array of the wavefront camera with lenses L_2 and L_3 . An estimate of the psf of the telescope and atmosphere is constructed from this digital image.

A brass board version of the system diagrammed in Fig. 1 was designed and assembled at the Weapons Laboratory. This instrument was then mounted on the University of New Mexico's astronomical telescope at the Capilla Peak Observatory. The telescope is a 24-in. $f/15.2$ Cassegrain. The beam splitter used in our setup reflects a $20\text{-}\mu\text{m}$ FWHM band of light centered at $0.63\text{ }\mu\text{m}$ to the focal plane. The combination of lenses L_1 and L_4 (Fig. 1) in our system results in an effective $f/\text{No.}$ of $f/60$ for the focal plane leg. A low noise CCD camera with 512×512 pixels and a pixel size of $19 \times 19\text{ }\mu\text{m}$ was used to record the focal plane images. The effective resolution of the focal plane system was, therefore, $0.109\text{ sec of arc/pixel}$, and the field of view was 55 sec of arc . The diffraction-limited angular resolution of the 24-in. telescope at a wavelength of $0.63\text{ }\mu\text{m}$ was $\sim 0.26\text{ sec of arc}$. Thus a diffraction-limited spot extends across ~ 2 pixels on the focal plane camera.

Our wavefront sensor consists of a square array of microscopic spherical lenslets. Each lenslet is $100\text{ }\mu\text{m}$ in diameter with a $135\text{-}\mu\text{m}$ center-to-center separation. The telescope exit pupil is reimaged to span a 64×64 array of these lenslets. A low noise CCD camera (512×512 pixels) is used to record the focal spots produced by the lenslet array.

We now present what to our knowledge are the first successful images of astronomical objects using post detection deconvolution. We observed several stars, collecting almost 1000 short exposure image-atmosphere pairs.

Figure 2 shows the results of SRS observations conducted 9 Feb. 1990 of α Aurigae (Capella), a bright star of visual magnitude of 0.08.¹⁵ The image (A) is the focal plane image with no correction. (B) shows the estimated psf obtained from the wavefront sensor. For a point source such as a star,

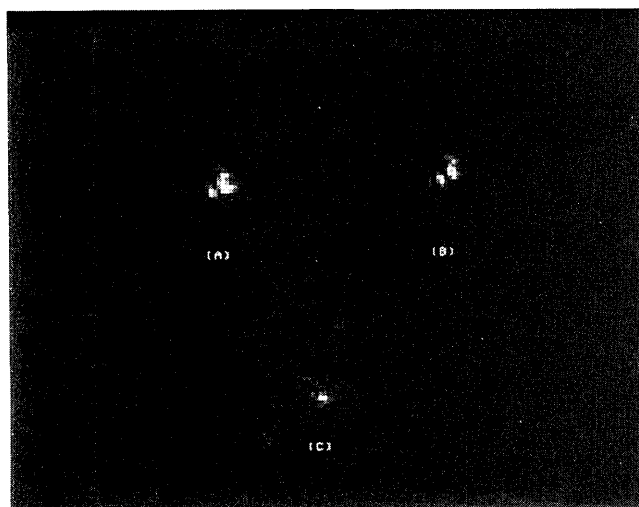


Fig. 2. α Aurigae image: (A) focal plane image; (B) atmospheric psf estimate; (C) compensated image.

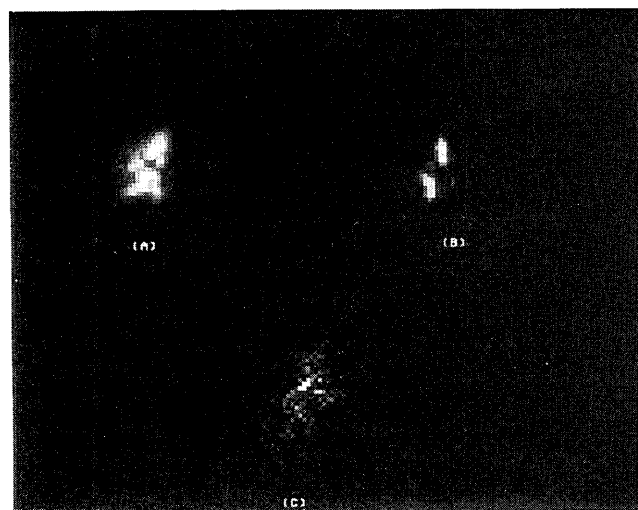


Fig. 3. ν Ursae Majoris image: (A) focal plane image; (B) atmospheric psf estimate; (C) compensated image.

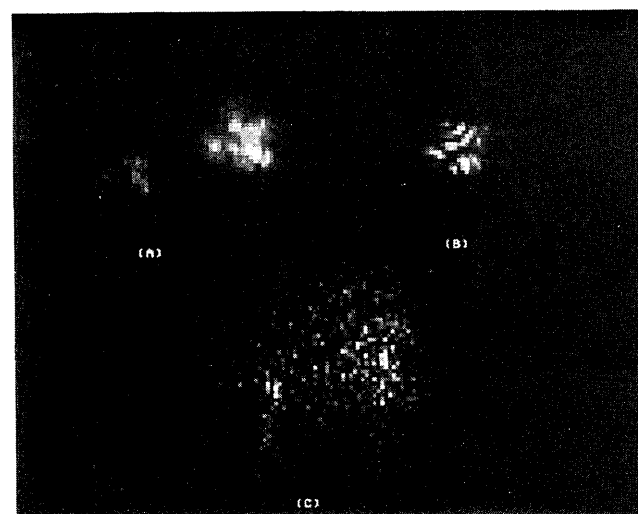


Fig. 4. α Geminorum image: (A) focal plane image; (B) atmospheric psf estimate; (C) compensated image.

the degraded image and psf should be identical. (C) then shows the image resulting from deconvolving the psf from the focal plane image. The exposure time was 10 ms, and we estimated Fried's r_0 parameter to be 7 cm. The restored image has virtually diffraction-limited resolution. Using the Strehl ratio as an image quality metric, we calculated the Strehl ratios of the uncorrected as 0.4 and that of the corrected image as 0.75. Note the lack of an Airy pattern in the reconstructed images because the deconvolution process removes the combined atmosphere and telescope transfer function.

The results of SRS measurements collected 12 Feb. 1990 of the dimmer star ν Ursae Majoris (Alula Borealis) are presented in Fig. 3. This star has a visual magnitude of 3.5.¹⁵ We estimate the r_0 parameter for these measurements at 5 cm. The exposure time was 60 ms, which was longer than the correlation time of the atmosphere. Some blurring of the speckles in the focal plane can be noted. The resulting restored image is slightly less than diffraction-limited. The calculated Strehl ratios for uncorrected and restored images are 0.09 and 0.6, respectively.

Finally, the results from observations also on 12 Feb. 1990 of the binary star system α Geminorum (Castor) are shown in Fig. 4. The system is composed of a 2.0 and 2.9 magnitude pair with a combined visual magnitude of 1.6.¹⁵ We estimated the atmospheric seeing at ~ 4 cm and used a long exposure time of 30 ms. This is longer than the correlation time of the atmosphere, and the speckles in the focal plane are quite blurred. The restored image shows considerable noise. The reconstructed image has a resolution less than the diffraction limit. However, it shows improvement over the uncorrected focal plane image. The angular separation of the two star systems measured from the reconstructed image is ~ 3.0 sec of arc, which closely agrees with the tabulated values.¹⁶

It is emphasized that the reconstructions shown in this Communication were obtained from single focal plane/psf pair measurements. The results illustrate the fact that this technique does not require the large number of exposures typical of white light speckle imaging techniques such as Knox-Thompson. Averaging snapshot spectra will, however, improve performance, especially for dimmer objects.

The authors wish to thank the University of New Mexico's Physics and Astronomy Department and in particular Dr. Neb Durik and Mr. John Dolby for their special support of the experiment at Capilla Peak. We also wish to thank Ms.

Kathy Schulze of Applied Technology Associates for her work in successfully fielding the experiment.

References

1. H. W. Babcock, "The Possibility of Compensating Astronomical Seeing," *Astron. Soc. Pac.* **65**, 229–236 (1953).
2. J. W. Hardy, J. E. Lefebvre, and C. L. Koliopoulos, "Real-Time Atmospheric Compensation," *J. Opt. Soc. Am.* **67**, 360–369 (1977).
3. A. Labeyrie, "Attainment of Diffraction Limited Resolution in Large Telescopes by Fourier Analyzing Speckle Patterns in Star Images," *Astron. Astrophys.* **6**, 85–87 (1975).
4. J. C. Dainty, "Stellar Speckle Interferometry," in *Laser Speckle and Related Phenomena*, J. C. Dainty, Ed. (Springer-Verlag, Berlin, 1975), pp. 253–315.
5. K. T. Knox and B. J. Thompson, "Recovery of Images from Atmospherically Degraded Short Exposure Photographs," *Astrophys. J.* **193**, L45–L48 (1974).
6. Y. C. Liu and A. W. Lohmann, "High Resolution Image Formation Through the Turbulent Atmosphere," *Opt. Commun.* **8**, 372–377 (1973).
7. R. Bates, P. Gough, and P. Napier, "Speckle Interferometry Gives Holograms of Multiple Star Systems," *Astron. Astrophys.* **22**, 319–320 (1973).
8. G. P. Weigelt, "Speckle Holography Measurements of Stars Zeta Cancri and ADS 3358," *Appl. Opt.* **17**, 2660–2662 (1978).
9. J. Fontanella, "Analyse de Surface D'onde, Deconvolution et Optique Active," *J. Opt. Paris* **16**, 257–268 (1985).
10. D. Fried, "Post Detection Wavefront Compensation," *Proc. Soc. Photo-Opt. Instrum. Eng.* **828**, 127–133 (1987).
11. D. Fried, "Statistics of a Geometric Representation of Wavefront Distortion," *J. Opt. Soc. Am.* **55**, 1427–1435 (1965).
12. B. L. McGlamery, "Restoration of Turbulence-Degraded Images," *J. Opt. Soc. Am.* **57**, 293–297 (1966).
13. B. L. McGlamery, "Computer Simulations Studies of Compensation of Turbulence Degraded Images," *Proc. Soc. Photo-Opt. Instrum. Eng.* **74**, 225–233 (1974).
14. J. Primot, G. Rousset, and J. Fontanella, "Deconvolution from Wavefront Sensing: A New Technique for Compensating Turbulence-Degraded Images," (unpublished).
15. D. Hoffleit, *The Bright Star Catalogue* (Yale U. P., New Haven, CT, 1982), pp. 72, 178, 118.
16. R. B. Burnham, *Burnham's Celestial Handbook* (Dover, New York, 1978), p. 917.

Performance of multilayer coated diffraction gratings in the EUV

Ritva A. M. Keski-Kuha, Roger J. Thomas, Jeffrey S. Gum, and Charles E. Condor

NASA Goddard Space Flight Center, Greenbelt, Maryland 20771

Received 22 May 1990.

Sponsored by William R. Hunter, Springfield, VA.

Performance of multilayer coated diffraction gratings has been evaluated in the extreme UV. The application of multilayer coatings to two blazed gratings has produced a significant enhancement in grating efficiency in the 300-Å spectral region in first order.

In the extreme ultraviolet (EUV) spectral region the low normal incidence reflectance of all conventional coatings

limits the throughput of EUV space astronomy instrumentation that use normal incidence components. However, the development of multilayer coatings with enhanced normal incidence reflectance allows us to take advantage of the conventional normal incidence mirror technology in the EUV. An extensive amount of work has already been done on applying multilayer coatings to mirrors for both laboratory and astronomical applications in sounding rocket experiments.^{1–10} It is also desirable to apply this technology to diffraction gratings to provide gratings with enhanced efficiency at normal incidence in wavelength regions where only glancing incidence designs have provided acceptable throughput.

Application of multilayer coatings to diffraction gratings for use in the spectral region below 200 Å has been studied by several investigators.^{11–15} They have demonstrated that multilayer coatings can provide gratings with enhanced effi-

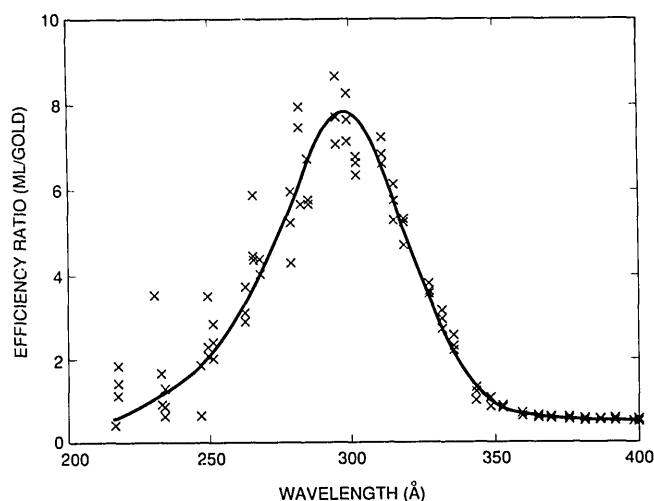


Fig. 1. Enhancement in first-order efficiency for the SERTS grating.

ciency over a narrow bandpass. Enhancement has also been demonstrated in the 300-Å spectral region for a sinusoidal grating.³ This paper discusses application of a multilayer coating to two diffraction gratings, 3600- and 1200-line/mm blazed replica gratings, designed for operation in the 300-Å spectral region in first order.

The 3600-line/mm 1.2-m toroidal tripartite grating with a blaze angle of 2.8° was developed for the solar extreme ultraviolet rocket telescope and spectrograph (SERTS) instrument.¹⁶ The optical system of this instrument consists of a Wolter type II glancing incidence telescope and a toroidal grating spectrograph operating at normal incidence. The grating selected was a flight spare replica with no special processing for a multilayer coating. This large format, a 9.5 × 8.5-cm gold coated grating, was fabricated by Hyperfine, Inc., with the ruled area 8.0 × 6.5 cm.

The ten-layer IrSi multilayer optimized for 304 Å was deposited using e-beam evaporation in a 2-m diam evaporator¹⁷ at GSFC. The multilayer coating, starting with silicon, was deposited directly on the gold coating. Four 5 × 5-cm microscope slides were mounted next to the grating. The grating and microscope slides were located 83 cm above the source, and the center of the grating was offset 9 cm from the center of the source. Based on distribution studies, the layer thickness uniformity across the grating was ~2%. The reflectance of the coating was measured on the microscope slides using a reflectometer-monochromator system described elsewhere.¹⁸ At a 15° angle of incidence the reflectance varied from 15.0 to 15.3% on the four microscope slides with the slide located farthest from the source having the highest reflectance of 16.1% at 12° angle of incidence. This is the smallest angle that can be measured due to instrument limitations.

The grating efficiency was measured on the SURF II calibration beamline at the National Institute of Standards and Technology (NIST) in a chamber that was designed for calibrating the SERTS gratings. The undispersed beam from the synchrotron beamline is incident on the grating at 7° angle of incidence. A calibrated photodiode detector is scanned through the wavelengths of interest in the dispersed beam. The incident flux at each wavelength is determined by the beam current and voltage in the storage ring. Figure 1 shows the measured efficiency ratio of the grating before and

after the multilayer coating in first order at nine different locations across the grating. The solid line represents an approximate average to the efficiency ratio data. The efficiency is enhanced by a factor of 7 in the 300-Å region. A factor of 4 or higher enhancement was achieved over a 50-Å bandpass. The ratio is quite uniform over the nine different locations across the grating. The result has important implications for future instrument applications, such as the Coronal Diagnostics Spectrometer¹⁹ on the SOHO mission.

A second grating coated with the SERTS grating was a replica 1200-line/mm concave grating with a radius of curvature of 1 m and blazed at 304 Å. This grating was fabricated by Hyperfine and had an aluminum/SiO_x coating. The purpose of the aluminum coating was to reject heat during the multilayer coating process, thereby preventing damage to the groove structure of the grating. The aluminum was overcoated with SiO_x to prevent a potential interdiffusion between aluminum and iridium. The ten-layer IrSi multilayer coating was deposited on a five-layer IrSi multilayer that had been deposited on the aluminum/SiO_x base coating earlier. The efficiency was measured at 304 Å at GSFC using the reflectometer-monochromator system mentioned earlier. An absolute efficiency of 4.8% in first order was achieved for this grating at 304 Å. This is a factor of 4 enhancement over the efficiency measured with an Ir coating.

In summary, the use of multilayer coatings on diffraction gratings has produced a significant enhancement in grating efficiency in the 300-Å spectral region. This implies that a significant improvement in throughput can be achieved in EUV instruments like SERTS that use gratings at normal incidence. Additional studies are in progress to compare the spectral resolution and absolute efficiency for the SERTS flight-spare grating with values established prior to depositing the multilayer coating. Preliminary data indicate that the grating suffered no loss in its excellent spectral resolution.

References

1. E. Spiller, "Reflective Multilayer Coatings for the Far UV Region," *Appl. Opt.* **15**, 2333 (1976).
2. J. H. Underwood and T. W. Barbee, Jr., "Layered Synthetic Microstructures as Bragg Diffractors for X Rays and Extreme Ultraviolet: Theory and Predicted Performance," *Appl. Opt.* **20**, 3027 (1981).
3. R. A. M. Keski-Kuha, "Layered Synthetic Microstructure Technology Considerations for the Extreme Ultraviolet," *Appl. Opt.* **23**, 3534 (1984).
4. T. W. Barbee, Jr., S. Mrowka, and M. C. Hettrick, "Molybdenum-Silicon Multilayer Mirrors for Extreme Ultraviolet," *Appl. Opt.* **24**, 883 (1985).
5. J. F. Meekins, R. G. Cruddace, and H. Gursky, "Optimization of Layered Synthetic Microstructures for Narrowband Reflectivity at Soft X-Ray and EUV Wavelengths," *Appl. Opt.* **25**, 2757 (1986).
6. J. F. Lindblom, A. B. C. Walker, Jr., R. B. Hoover, T. W. Barbee, Jr., R. A. van Patten, and J. P. Gill, "Soft X-Ray/Extreme Ultraviolet Images of the Solar Atmosphere with Normal Incidence Multilayer Optics," *Proc. Soc. Photo-Opt. Instrum. Eng.* **982**, 324 (1988).
7. B. M. Haisch, T. E. Whittmore, E. G. Joki, W. J. Brookover, and G. J. Rottman, "A Multilayer X-Ray Mirror for Solar Photometric Imaging Flown on a Sounding Rocket," *Proc. Soc. Photo-Opt. Instrum. Eng.* **982**, 38-45 (1988).
8. R. C. Catura and L. Golub, "XUV Multilayered Optics for Astrophysics," *Rev. Phys. Appl.* **23**, 1741-1746 (1988).

9. A. B. C. Walker, T. W. Barbee, R. B. Hoover, and J. F. Lindblom, "Soft X-Ray Images of the Solar Corona with a Normal Incidence Cassegrain Multilayer Telescope," *Science* **241**, 1781-1787 (1989).
10. L. Golub *et al.*, "Sub-arcsecond Observations of the Solar X-ray Corona," *Nature London* **344**, 842-844 (1990).
11. J. C. Rife, W. R. Hunter, T. W. Barbee, Jr., and R. G. Cruddace, "Multilayer-Coated Blazed Grating Performance in the Soft X-Ray Region," *Appl. Opt.* **28**, 2984-2986 (1989).
12. T. W. Barbee, "Combined Microstructure X-Ray Optics," *Rev. Sci. Instrum.* **260**, 1588 (1989).
13. J. C. Rife, T. W. Barbee, W. R. Hunter, and R. G. Cruddace, "Performance of a Tungsten/Carbon Multilayer-Coated Blazed Grating from 150 to 1700 eV," *Phys. Scr.* **41**, 418 (1990).
14. R. G. Cruddace, T. W. Barbee, J. C. Rife, and W. R. Hunter, "Measurements of the Normal-Incidence X-Ray Reflectance of a Molybdenum-Silicon Multilayer Deposited on a 200 l/mm Grating," *Phys. Scr.* **41**, 396 (1990).
15. J. V. Bixler, T. W. Barbee, and D. D. Dietrich, "Performance of Multilayer Coated Gratings in the Extreme Ultraviolet," *Proc. Soc. Photo-Opt. Instrum. Eng.* **1160**, 648-654 (1989).
16. W. M. Neupert, G. L. Epstein, R. J. Thomas, and U. Feldman, "A Solar Ultraviolet Telescope and Spectrograph for Shuttle/Spacelab," *Space Sci. Rev.* **29**, 425-429 (1981).
17. A. P. Bradford, G. Hass, J. F. Osantowski and A. R. Toft, "Preparation of Mirror Coatings for the Vacuum Ultraviolet in the 2-m Evaporator," *Appl. Opt.* **8**, 1183 (1969).
18. J. F. Osantowski, "Reflectance and Optical Constants for Cer-Vit from 250 to 1050 Å," *J. Opt. Soc. Am.* **64**, 834 (1974).
19. B. E. Patchett *et al.*, "CDS—The Coronal Diagnostic Spectrometer," *The SOHO Mission—Scientific and Technical Aspects of the Instruments*, ESA SP-1104 (1989), pp. 39-42.

In-focus monochromator: theory and experiment of a new grazing incidence mounting

Michael C. Hettrick

Hettrick Scientific, Inc., P.O. Box 8046, Kensington, California 94707.

Received 6 June 1990.

Sponsored by William R. Hunter, Springfield, Virginia.

0003-6935/90/314531-05\$02.00/0.

© 1990 Optical Society of America.

A varied-space grating mounted to both rotate and translate constitutes a practical single element fixed slit monochromator which is in focus at all wavelengths. Keywords: Monochromators, diffraction gratings, grazing incidence, x-ray optics.

No self-focusing reflection grating has hitherto delivered spectral images which remain in focus to first power in the aperture over a continuum of wavelengths diffracted between fixed entrance and exit slits. Rowland circle designs^{1,2} require movable slits, whereas plane grating monochromators employ auxiliary mirrors³⁻⁷ which lower the throughput and introduce figuring and alignment errors. Fixed slit designs where a concave grating simply rotates to select the wavelength are practically in focus at near normal incidence⁸ but suffer from severe defocusing at grazing incidence.^{3,9}

These limitations are overcome with a new optical design, whose essential features are shown in Fig. 1. A reflection grating consists of grooves whose spacings vary continuously across its ruled width. To select the desired transmitted wavelength, the grating is rotated about an axis fixed in space, while simultaneously being translated along its surface in the direction of its ruled width. Due to the varied spacing, the translation provides a new set of effective grating parameters where the principal ray strikes the grating surface. The freedom to choose the amount of translation permits each wavelength to be brought into an exact focus (to first power) at the fixed exit slit. The novelty of this scheme may be appreciated from the fact that such a translation would have no effect on the properties of a conventional (equally spaced) grating.

This degree of freedom inherent in varied-space gratings has previously been left unexploited, except for theoretical

designs requiring a prohibitively large exponential variation in spacing.¹⁰ The combined rotation and translation of a (varied-space) grating is a new mounting; hence the grating itself must be derived from a new focusing condition rather than as an improvement in any classical grating.

The extent to which the optical aberrations are controlled is best analyzed if the local groove density of the grating is expanded as a power series in the grating aperture:

$$1/\sigma = 1/\sigma_0 + N_2w + N_3w^2 + N_4w^3 + \dots, \quad (1)$$

where σ_0 is the nominal groove spacing at the grating center ($w = 0$); N_2, N_3, N_4 , etc. are varied-space constants; and w is the ruled width coordinate as projected on the plane tangent to the grating at its center.

The wavelength diffracted through an infinitesimally narrow exit slit by the grooves in the vicinity of coordinate w will differ from that diffracted by the grating center by an amount

$$\Delta\lambda = (\sigma_0/m)(F_2/w + \frac{1}{2}F_3w^2 + 2F_4w^3 + \dots), \quad (2)$$

where m is the spectral order, and F_2, F_3, F_4 , etc. are the Fermat aberration coefficients. The image is considered to be in-focus at the exit slit if the first power aberration $F_2 = 0$. Finite F_3 values result in a comatic image whose profile is asymmetrical, while the third power F_4 term is spherical aberration, present even along the classical Rowland circle. To minimize the total amount of translation required over a finite spectral region, we first consider rotation only of the grating to select two wavelengths, λ_1 and λ_2 , and adjust the design parameters to minimize the aberrations there. Even with the constraint of fixed slits, F_2 and F_3 may be made to vanish at both wavelengths if the grating is concave ($0 < R < \infty$), resulting in the following focusing condition:

$$1/r = (\sqrt{b^2 - 4ac} - b)/(2aR), \quad (3)$$

$$1/r' = \delta/r - \epsilon/R, \quad (4)$$

$$N_2 = (T_1 + T'_1)/(m\lambda_1), \quad (5)$$

$$N_3 = \frac{3}{2}[T_1(\sin\alpha_1)/r - T'_1(\sin\beta_1)/r']/(m\lambda_1), \quad (6)$$

where $T = (\cos^2\alpha)/r - (\cos\alpha)/R$, $T' = (\cos^2\beta)/r' - (\cos\beta)/R$,

$$a = \gamma \sin\alpha_1 \cos^2\alpha_1 - \sin\alpha_2 \cos^2\alpha_2 - \gamma\delta^2 \sin\beta_1 \cos^2\beta_1 + \delta^2 \sin\beta_2 \cos^2\beta_2, \quad (7)$$

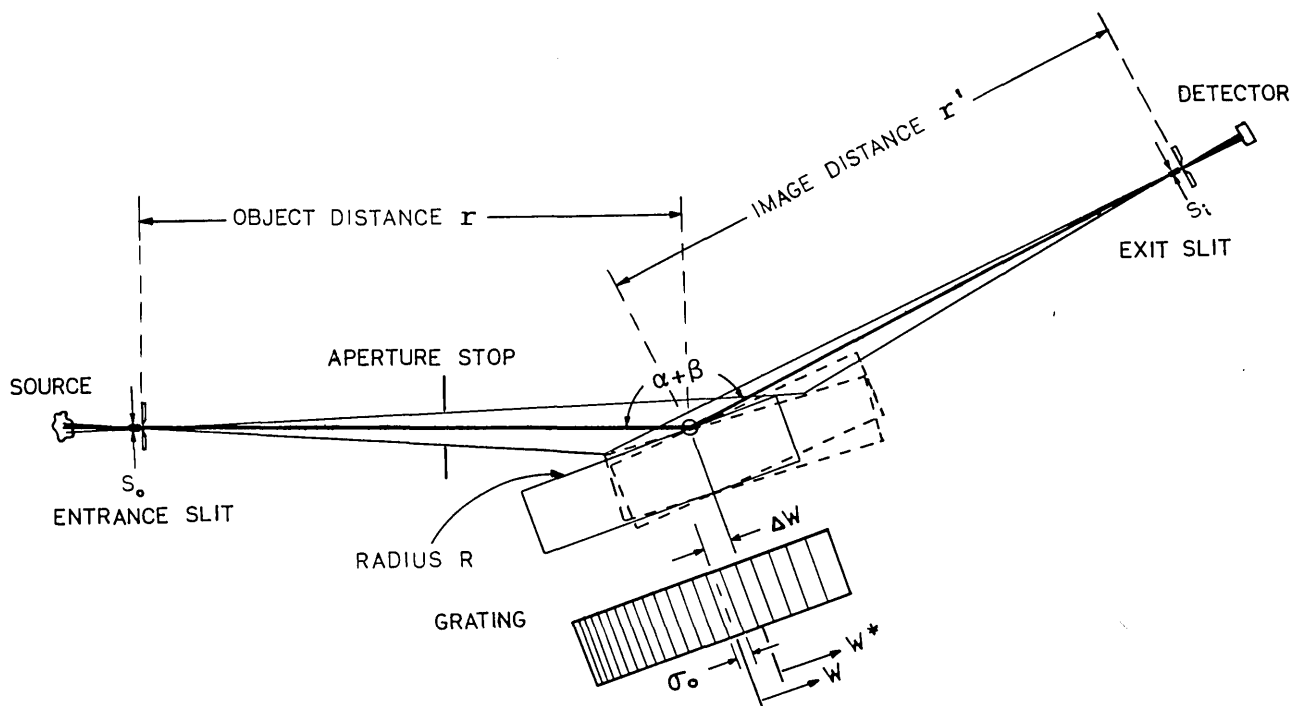


Fig. 1. Basic optical configuration of the monochromator. The upper portion shows a section taken across the meridional plane of the grating. A reflection grating rotates about a fixed axis (open circle) while translating along its surface in the direction of its varied groove spacing. The fixed principal ray is indicated by dark lines. The grating position is drawn solid for a typical wavelength and dashed for two extreme wavelengths at opposite ends of the spectral range of a concave grating embodiment. The bottom portion is a top view of the grating surface, schematically showing the varied spacing.

$$b = -\gamma \sin \alpha_1 \cos \alpha_1 + \sin \alpha_2 \cos \alpha_2 + 2\gamma \delta \epsilon \sin \beta_1 \cos^2 \beta_1 - 2\delta \epsilon \sin \beta_2 \cos^2 \beta_2 + \gamma \delta \sin \beta_1 \cos \beta_1 - \delta \sin \beta_2 \cos \beta_2, \quad (8)$$

$$c = -\gamma \epsilon^2 \sin \beta_1 \cos^2 \beta_1 + \epsilon^2 \sin \beta_2 \cos^2 \beta_2 - \gamma \epsilon \sin \beta_1 \cos \beta_1 + \epsilon \sin \beta_2 \cos \beta_2, \quad (9)$$

$$\delta = (\gamma \cos^2 \alpha_1 - \cos^2 \alpha_2) / (\cos^2 \beta_2 - \gamma \cos^2 \beta_1), \quad (10)$$

$$\epsilon = [\gamma (\cos \alpha_1 + \cos \beta_1) - (\cos \alpha_2 + \cos \beta_2)] / (\cos^2 \beta_2 - \gamma \cos^2 \beta_1), \quad (11)$$

$$\gamma = \lambda_2 / \lambda_1, \quad (12)$$

where R is the grating radius of curvature, r is the object distance, r' is the image distance, and α and β are the angles of incidence and diffraction, respectively, relative to the grating surface normal. All values are measured from the fixed axis of rotation, which for simplicity is assumed to intersect the grating at its center.

For example, a design tailored to extreme UV wavelengths may have as input parameters $\sigma_0 = 1/1500$ mm, $R = 10$ m, constant deviation $\alpha + \beta = 164^\circ$, $m = +1$, $\lambda_1 = 100$ Å, and $\lambda_2 = 200$ Å. Equations (3)–(12) then provide the design parameters $r = 1011.488$ mm, $r' = 964.542$ mm, $N_2 = -1.63766$ mm⁻², and $N_3 = +0.00267255$ mm⁻³. These differ substantially from those of a conventional concave grating monochromator.

Using the above parameters and a 50-mm illuminated aperture, curves 200, 202, and 204 of Fig. 2 are the individual optical aberrations of Eq. (2) with only grating rotation to select the wavelength. As constrained above, the resolution

is extremely high in the immediate vicinity of the two wavelengths, λ_1 and λ_2 . However, it degrades rapidly elsewhere, dominated by a large amount of defocusing (curve 200). The maximum defocus of 0.5 Å is nearly as poor as the 0.7 Å resulting from an equally spaced grating design⁹ of the same aperture, system length, angular deviation, and groove density (curves 100, 102, and 104).

The key to removal of defocusing aberrations, and hence the usefulness of the present grating design, is a translation of the grating at all wavelengths other than λ_1 and λ_2 . Considering simple linear translation in the direction of the tangent plane at the grating center results in the following substitutions:

$$w \rightarrow w^* = w - \Delta w, \quad (13)$$

$$1/\sigma_0 \rightarrow 1/\sigma_0^* = 1/\sigma_0 (1 - \frac{1}{2}\phi^2) + N_2 \Delta w (1 - \frac{2}{3}\phi^2) + N_3 \Delta w^2 + N_4 \Delta w^3, \quad (14)$$

$$N_2 \rightarrow N_2^* = -\phi/(R\sigma_0) + N_2(1 - 2\phi^2) + 2N_3 \Delta w + 3N_4 \Delta w^2, \quad (15)$$

$$N_3 \rightarrow N_3^* = -\phi^2/(4R^2\sigma_0) - \frac{3}{2}N_2(1 + \frac{2}{9}\phi^2)\phi/R + N_3(1 + \frac{1}{2}\phi^2) + 3N_4(1 + \frac{1}{6}\phi^2)\Delta w, \quad (16)$$

$$N_4 \rightarrow N_4^* = -\frac{2}{3}\phi/R^3\sigma_0 - \frac{4}{3}N_2(\phi/R)^2 + \frac{4}{3}N_3\phi/R + N_4(1 + 2\phi^2), \quad (17)$$

where

$$\phi = \arcsin(\Delta w/R), \quad (18)$$

Δw being the amount of translation in the direction of the decreasing ruled width. The fixed principal ray now strikes

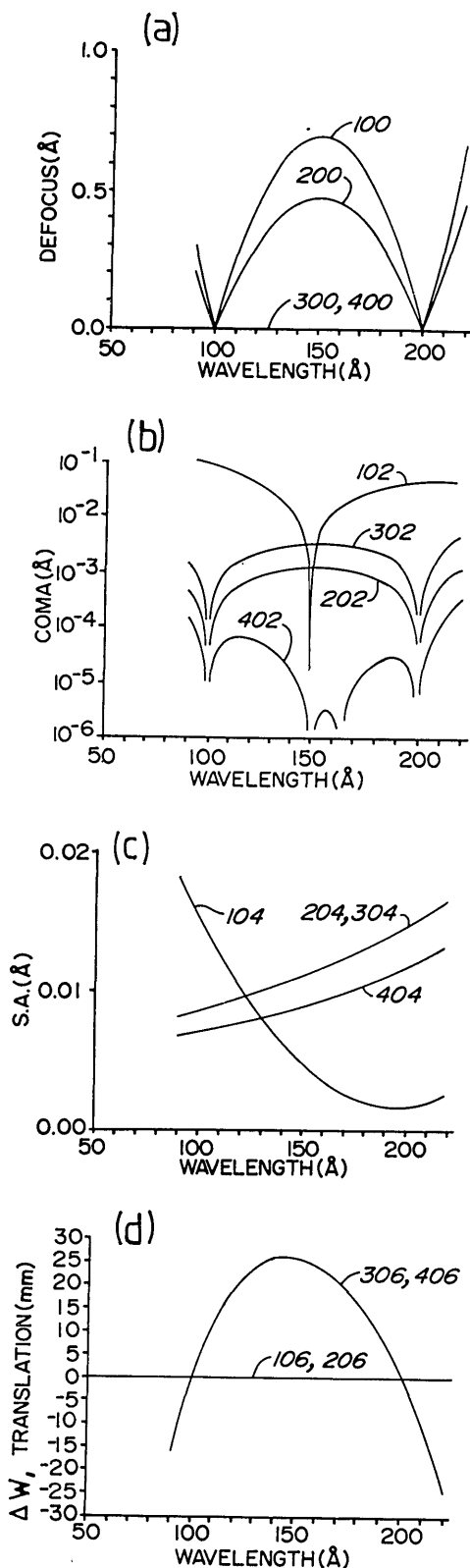


Fig. 2. Results of Fermat calculations using parameters for a grazing incidence monochromator: (a) first-order aberration of defocusing; (b) second-order aberration of coma; (c) third-order spherical aberration; and (d) grating surface translation. Curves 100–106 are for a classical equally spaced spherical grating, which simply rotates about its pole to select the wavelength. Curves 400–406 are optimized for the new focusing condition, where a varied-space concave grating rotates about a fixed pole and translates along its ruled width. Given the same grating width, the new device exhibits a factor of 200 higher spectral resolution, limited only by spherical aberration. All aberrations are extrema (calculated from the edge of the grating aperture).

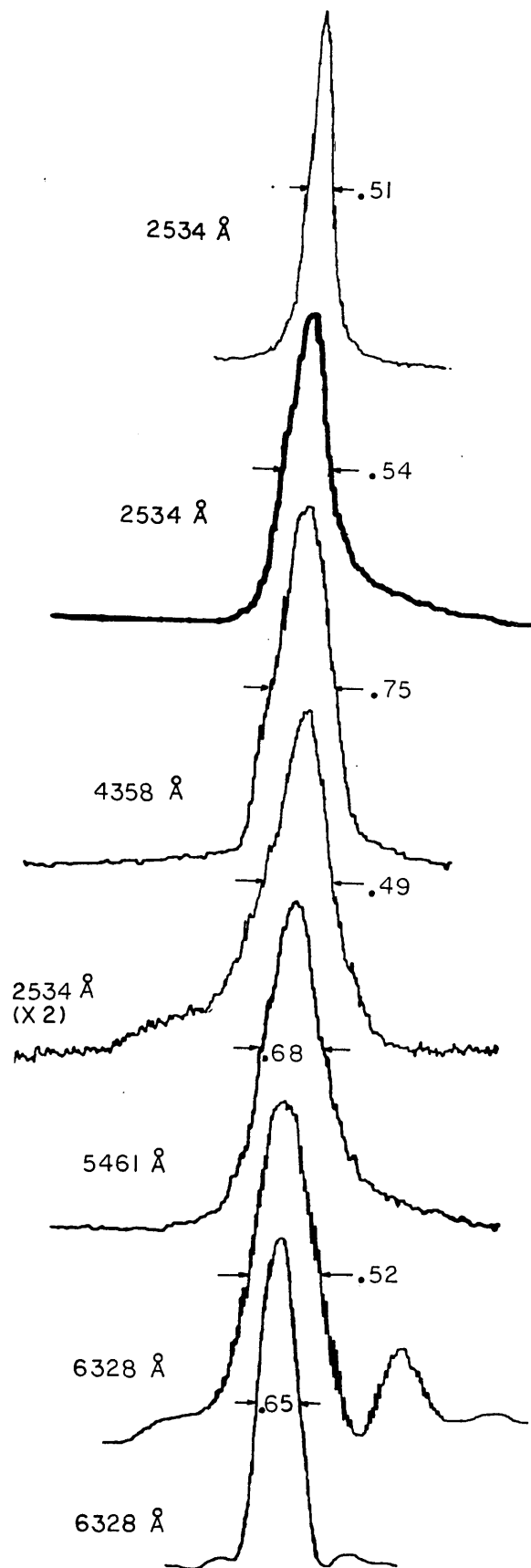


Fig. 3. Measured line profiles of a prototype in-focus monochromator, employing a single spherical grating reflection. Typical slit widths were 5–10 μm . These traces are not plotted on the same scale; however, the measured FWHM is indicated for each profile. The full grating aperture of 45 mm was used for all traces, except for the top and bottom traces where the aperture was stopped to ~ 36 mm to provide a centered illumination.

the ruled width coordinate $w = \Delta w$, and w^* is measured relative to this new pole.

Using the same numerical parameters previously given and choosing $N_4 = 0$, curves 300, 302, and 304 of Fig. 2 result from numerically iterating Eqs. (14), (15), and (18) to eliminate defocusing at all wavelengths. All wavelengths are now sharply in focus, the new limit to the optical resolution being spherical aberration. As this term is proportional to the third power of the grating aperture, ~63% of the total diffracted energy is enclosed within an image width which is only one-fourth of the extreme aberration plotted in Fig. 2(c). The resulting spectral resolution is thus ~0.003 Å.

A further correction is available by use of nonzero values for N_4 . From Eq. (16) it is clear that this term will significantly change the substituted value of N_3^* as the grating is translated ($\Delta w \neq 0$). Curve 402 reveals the elimination of the coma at a third wavelength near the spectrum center by the choice of $N_4 = -6.99 \times 10^{-7} \text{ mm}^{-4}$. In practice the coma becomes negligible at all wavelengths, resulting in a highly symmetrical image whose remaining spherical aberration (curve 404) may be deconvolved from a spectrum by the use of accurate modeling techniques.

Because the grating radius and rotation provide for the broad selection of wavelength, the amount of space variation required is small and easily accomplished with present technology. As plotted in Fig. 2(d), the maximum amount of translation is only 25 mm. A 75-mm ruled grating width, with an aperture stop (Fig. 1) to constrain an exactly fixed beam direction, will provide the assumed 50-mm illuminated aperture. Alternatively, the full 75 mm may be utilized at all wavelengths if the incident beam overilluminates the grating and a $\pm 15\%$ deviation is allowed in the direction of the ray diffracted from the center of the aperture.

The small amount of translation also enables the use of a simple linear translation stage, the resulting vertical movement of the intersection point of the concave grating surface with the principal ray being unimportant. This maintains fixed directions for the incident and diffracted rays. Furthermore, because the grating translation functions only to

remove a residual amount of defocusing, the required accuracy of translation is modest.

Experimental verification of the above new theory has been accomplished by construction of a breadboard developmental version of this monochromator. To demonstrate the grazing incidence performance and hence the applicability of this design to short wavelengths, the included angle ($\alpha + \beta$) of the principal ray was chosen to be 140° (20° graze at zero order). The numerical parameters were chosen to enable operation in the ultraviolet and visible regions of the spectrum so as to allow alignment and testing in atmosphere. The resulting groove density was 200 g/mm at the grating center, the radius of curvature of the spherical grating was 1001 mm, the object distance was 301.5 mm, image distance was 316.6 mm, and the full grating aperture was 45 mm. For this demonstration, the grating translation was provided by a manual micrometer and ball slide, and the rotation driven by a precision lead screw and wavelength bar. At each wavelength tested, the translation was experimentally adjusted to maximize the detected power. Then a high resolution scan across the spectral line was traced on a chart recorder. Two light sources were used: a low pressure mercury lamp and a He-Ne laser. The mercury discharge was ~5 mm in diameter and placed behind the entrance slit, whereas the collimated laser pencil beam ~0.6 mm in diameter was simply diffracted by the entrance slit to illuminate the full grating aperture.

Figure 3 shows the wavelength profiles obtained for three strong emission lines of the Hg lamp and the red line of the He-Ne laser. These traces reveal a symmetrical centrally peaked in-focus image at each wavelength. As listed in Table I, which includes an additional three (weaker) Hg lines, all measured resolutions are attributed entirely to either the finite slit widths or the physical diffraction-limited resolution (9000 grooves full aperture). In agreement with both geometrical (Fermat) calculations and numerical ray tracing of the line profiles, the obtained resolution of <1 Å is approximately a factor of 4 less than the extremum spherical aberration calculated to be 3–5 Å for wavelengths of 2534 to

Table I. Predicted and Measured Monochromator Performance^a

m	$\lambda(\text{Å})$	$\Delta w(\text{mm})$ Theory	$\Delta w(\text{mm})$ Actual	$\Delta\lambda_d(\text{Å})$	$s_0(\mu\text{m})$	$s_i(\mu\text{m})$	$\Delta\lambda_0(\text{Å})$	$\Delta\lambda_i(\text{Å})$	$\Delta\lambda(\text{Å})$ Actual
	Uncertainty (\pm)		0.2		1	1	0.08	0.05	0.05
1	2534	0.00	0.12	0.28	10	10	0.68	0.88	0.82
1	2534			0.28	10	5	0.68	0.22	0.73
1	2534			0.36 ^b	5	5	0.34	0.22	0.51
1	3126	6.10	6.30	0.35	20	20	1.41	0.81	1.35
1	3126			0.35	10	10	0.70	0.40	0.75
1	3650	8.39	8.37	0.41	20	20	1.46	0.76	1.35
1	4047	8.86	8.82	0.45	10	10	0.75	0.36	0.72
1	4358	8.88	8.67	0.48	10	10	0.76	0.35	0.75
2	2534	6.84	6.52	0.14	10	10	0.40	0.16	0.49
1	5461	5.14	4.97	0.61	10	10	0.81	0.30	0.68
1	5461			0.61	5	10	0.40	0.30	0.56
1	6328	0.00	0.00	0.70	10	5	0.85	0.13	0.64
1	6328			0.70	5	5	0.42	0.13	0.52
1	6328			0.87 ^b	10	5	0.85	0.13	0.65
1	6328			0.87 ^b	5	5	0.42	0.13	0.65

^a m , spectral order; λ , wavelength; Δw (theory), predicted grating translation; Δw (actual), measured grating translation relative to 0- μm reading for optimized imaging at $\lambda = 6328 \text{ Å}$; $\Delta\lambda_d$, diffraction-limited resolution, assuming a full grating aperture; s_0 , entrance slit width; s_i , exit slit width; $\Delta\lambda_0$, entrance slit-limited resolution; $\Delta\lambda_i$, exit slit-limited resolution; $\Delta\lambda$ (actual), measured FWHM of traced line profile.

^b Grating width stopped to 36 mm, centered at the rotation axis.

6328 Å. A few of the profiles in Fig. 3 can be seen to have a slightly higher wing to one side of the peak. This is due to the grating translation (9 mm, as given in Table I), which weights the aperture and thus the spherical aberration to one side of the grating pole. This effect is removed by stopping this small fraction of the aperture, resulting in the symmetrical profiles shown in the top and bottom traces of Fig. 3. The diffraction-limited profile at 6328 Å is evidenced by the presence of subsidiary maxima.

The measured FWHM of these profiles, using slit widths of 5–10 μm, represents resolving powers $\lambda/\Delta\lambda = 5000$ –12,000 for this grazing incidence monochromator of only 0.6 m in length and a meridional aperture of 0.05 rad. A conventional spherical grating would exhibit a defocusing of 35 Å at the center of this spectral region ($\lambda/\Delta\lambda = 125$).

The ability to maintain the spectral focus for large grating apertures provides higher throughput than previous designs,^{3,9} making the in-focus monochromator (IFM) particularly advantageous when operated with soft x-ray radiation. When used with conventional laboratory sources (electron bombardment, spark gap, Penning, and hollow cathodes), a single element IFM as discussed above is appropriate. However, to maintain bright images when operating with low emittance sources, such as laser-produced plasmas and synchrotron radiation, stigmatic versions of the monochromator are required. This may be accomplished without degradation of spectral resolution by the insertion of a mirror which provides focusing in the direction normal to the grating dispersion. For example, a 1-m long stigmatic IFM having a geometrical collection aperture of $\sim 1 \times 10^{-3}$ sr would provide an optical resolving power of 10^3 in the 35–500-Å wavelength region.

Commercial models of the IFM are being developed by Hettrick Scientific, Inc., which holds a license for manufacture, sale, and use of these devices. U.S. and foreign patents are pending on the general technique of combined rotation

and translation of a varied-space grating, one embodiment of which has been described in this Communication.

The author thanks George Hirst for fabrication of the grating and loan of a detector used in the measurements reported here.

References

1. H. A. Rowland, "On Concave Gratings for Optical Purposes," *Philos. Mag.* **16**, 197–210 (1883).
2. F. C. Brown, R. C. Bachrach, and N. Lien, "The SSRL Ultrahigh Vacuum Grazing Incidence Monochromator: Design Characteristics and Operating Experience," *Nucl. Instrum. Methods* **152**, 73–79 (1978).
3. M. C. Hettrick, "High Resolution Gratings for the Soft X-Ray," *Nucl. Instrum. Methods* **A266**, 404–413 (1988).
4. M. Itou, T. Harada, and T. Kita, "Soft X-Ray Monochromator with a Varied-Space Plane Grating for Synchrotron Radiation: Design and Evaluation," *Appl. Opt.* **28**, 146–152 (1989).
5. H. Dietrich and C. Kunz, "A Grazing Incidence Vacuum Ultraviolet Monochromator with Fixed Exit Slit," *Rev. Sci. Instrum.* **43**, 434–442 (1972).
6. W. R. Hunter, R. T. Williams, J. C. Rife, J. P. Kirkland, and M. N. Kabler, "A Grating/Crystal Monochromator for the Spectral Range 5 eV to 5 KeV," *Nucl. Instrum. Methods* **195**, 141–153 (1982).
7. H. Petersen, "The Plane Grating and Elliptical Mirror: A New Optical Configuration for Monochromators," *Opt. Commun.* **40**, 402–406 (1982).
8. T. Namioka, "Theory of the Concave Grating III. Seya-Namioka Monochromator," *J. Opt. Soc. Am.* **49**, 951–961 (1959).
9. M. C. Hettrick and J. H. Underwood, "Stigmatic High Throughput Monochromator for Soft X Rays," *Appl. Opt.* **25**, 4228–4231 (1986).
10. D. E. Aspnes, "High-Efficiency Concave-Grating Monochromator with Wavelength-Independent Focusing Characteristics," *J. Opt. Soc. Am.* **72**, 1056–1061 (1982).

Double-headed Dragon monochromator for soft x-ray circular dichroism studies

Chien-Te Chen, Francesco Sette, and Neville V. Smith

AT&T Bell Laboratories, Murray Hill, New Jersey 07974.
Received 4 June 1990.

Sponsored by William R. Hunter, Springfield, Virginia
0003-6935/90/314535-02\$02.00/0.

© 1990 Optical Society of America.

Efficient differentiation between the left and right circular polarization of soft x-ray synchrotron radiation is achievable by doubling the number of prefocusing mirrors in a Dragon monochromator. The design also permits easy reversion to conventional linear polarization operation.

An important property of synchrotron radiation from electron storage rings is the high degree of circular polarization just above or just below the plane of the ring.¹ In the vacuum ultraviolet (VUV) region, this property has been exploited in numerous spin-polarized photoemission studies.^{2,3} In the x-ray region, the number of circular polarization studies is still relatively sparse.^{4,5} To maximize the detection sensitivity, it is necessary to alternate between left and right circular polarization without affecting the position, energy resolution, or wavelength of the photon beam. In the VUV region ($h\nu \lesssim 30$ eV), where it is possible to work at normal incidence with large aperture gratings, this capability is readily achieved at the sample using masks and choppers.⁶ In the

hard x-ray region, an analogous approach can be employed because of the nongrazing incident angles of the photon beam on crystal monochromators and the small angular separation between beams of different polarization compared with the monochromator crystals' rocking curve.⁴ These approaches are not immediately transferable to the soft x-ray region, where the need for grazing incidence optics requires prohibitively long gratings.

Our Dragon monochromator⁷ at the National Synchrotron Light Source has recently been modified to perform circular dichroism studies without affecting its superior high resolution and flux performances.⁵ The modifications, illustrated in Fig. 1, involve laborious coordinated translations of the entrance slit and a vertical focusing mirror as well as a recalibration of the wavelength scale. This precludes rapid alternation between left and right circular polarization and imposes limits on the sensitivity of the measurements.

Our solution to this problem is the double-headed (DH) Dragon. The basic idea, illustrated in Fig. 2, is to replace the horizontal focusing mirror (HFM) and vertical focusing mirror (VFM) at the head of the original Dragon with two identical pairs of mirrors HFM₁, VFM₁ and HFM₂, VFM₂. In the configuration of Fig. 2(b), VFM₁ (VFM₂) intercepts radiation below (above) the plane of the ring. Both VFMs focus onto the fixed entrance slit and illuminate the grating at the same angle, so that the wavelength calibration and resolution are the same for both beams. Each beam is delivered simultaneously to the sample region, and the position of the two beams is identical in the vertical plane, while it can be

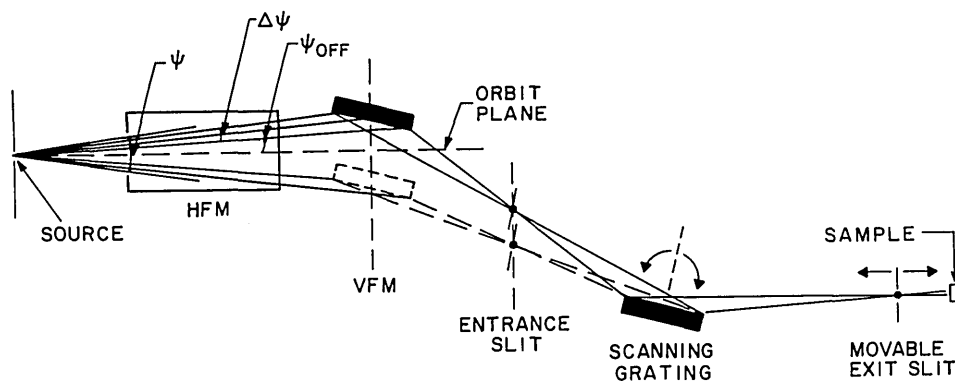
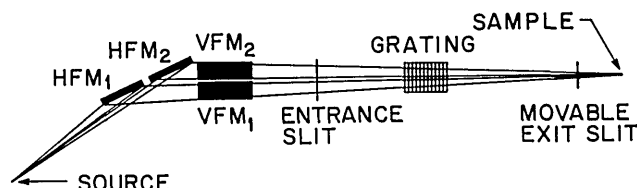
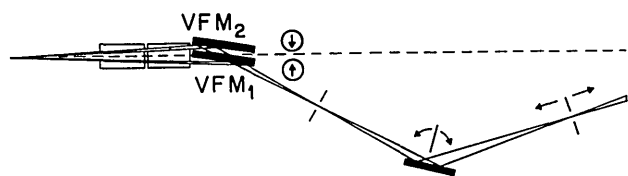


Fig. 1. Modification of the existing Dragon monochromator to select circularly polarized synchrotron radiation above and below the orbital plane of the storage ring. Concerted motions of the VFM and entrance slit are required, so that the alternation between left and right circular polarization is a cumbersome procedure.

(a) DOUBLE HEADED DRAGON (TOP VIEW)



(b) CIRCULAR POLARIZATION (SIDE VIEW)



(c) LINEAR POLARIZATION (SIDE VIEW)

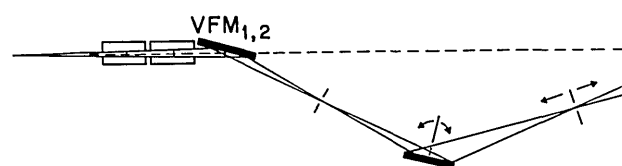


Fig. 2. Layout of the double-headed Dragon: (a) separation of the beam by identical pairs (HFM₁, VFM₁) and (HFM₂, VFM₂) of horizontal and vertical focusing mirrors; (b) circular polarization mode in which VFM₁ (VFM₂) intercept radiation below (above) the orbital plane; (c) conventional mode with both VFMs in the orbital plane.

arbitrarily adjusted in the horizontal plane by changing the incidence angles on HFM₁ and HFM₂. With this beamline configuration rapid (>100-Hz) alternation between left and

right circular polarization is accomplished using a lateral chopper before the entrance slit, as is evident from Fig. 2(a). Alternatively, simultaneous left and right circular polarization measurements are possible by either focusing separately on two samples or (where a transmission or reflection mode is feasible) using two separate detectors.

Conventional operation (i.e., linear polarization) may be retrieved simply by manipulating both VFMs into the orbital plane of the ring, as indicated in Fig. 2(c). Even here, the double-headed configuration offers advantages. First, an appropriate arrangement of the two half-length HFMs reduces the coma aberration by a factor of 4, improving the horizontal spot size at the sample position. Second, two smaller mirrors will usually be less expensive than a single large mirror.

In closing, we urge that future soft x-ray beamlines be built in the double-headed configuration to exploit fully the polarization properties of synchrotron radiation.

References

1. S. Krinsky, M. L. Perlman, and R. E. Watson, "Characteristics of Synchrotron Radiation and of Its Sources," in *Handbook on Synchrotron Radiation*, Vol. 1a, E. E. Koch, Ed. (North-Holland, Amsterdam, 1983), pp. 65-171.
2. U. Heinzmann, "Angle-, Energy- and Spin-Resolved Photoelectron Emission Using Circularly Polarized Synchrotron Radiation," *Phys. Scr.* T17, 77-88 (1987) and references therein.
3. J. Garbe and J. Kirschner, "Spin-Dependent Photoemission Intensities from Platinum(111)," *Phys. Rev. B* 39, 9859-9864 (1989) and references therein.
4. G. Schutz, R. Frahm, R. Wienke, W. Wilhelm, W. Wagner, and P. Kienle, "Spin-Dependent K- and L-Absorption Measurements," *Rev. Sci. Instrum.* 60, 1661-1665 (1989) and references therein.
5. C. T. Chen, F. Sette, Y. Ma, and S. Modesti, "Soft X-ray Magnetic Circular Dichroism at the L_{2,3} Edges of Nickel," submitted to *Phys. Rev. B*.
6. U. Heinzmann, "Spin Polarized Photoelectrons from Atoms and Molecules," *Appl. Opt.* 19, 4087-4091 (1980).
7. C. T. Chen, "Concept and Design Procedure for Cylindrical Element Monochromators for Synchrotron Radiation," *Nucl. Instrum. Methods A* 256, 595-604 (1987); C. T. Chen and F. Sette, "Performance of the Dragon Soft X-ray Beamline," *Rev. Sci. Instrum.* 60, 1616-1621 (1989).